Kilohertz volumetric imaging of in-vivo dynamics using squeezed light field microscopy

Zhaoqiang Wang[1,8], Ruixuan Zhao[1,8], Daniel A Wagenaar[2], Wenjun Kang[3], Calvin K. Lee[1,4,5,6], William C. Schmidt[1,4,5,6], Aryan Pammar[1], Enbo Zhu[7], Gerard C.L. Wong[1,4,5,6], Rongguang Liang[3], Tzung K. Hsiai[7], and Liang Gao[1,9]

[1]Department of Bioengineering, Henry Samueli School of Engineering and Applied Science, University of California, Los Angeles, Los Angeles, CA, USA.
[2]Division of Biology and Biological Engineering, Tianqiao and Chrissy Chen Institute for Neuroscience, California Institute of Technology, Pasadena, CA, USA
[3]Wyant College of Optical Science, University of Arizona, Tucson, AZ, USA
[4]Department of Chemistry and Biochemistry, University of California, Los Angeles, Los Angeles, CA, USA.
[5]California NanoSystems Institute, University of California, Los Angeles, Los Angeles, CA, USA.
[6]Department of Microbiology, Immunology, & Molecular Genetics, University of California, Los Angeles, Los Angeles, CA, USA.
[7]Division of Cardiology, Department of Medicine, David Geffen School of Medicine, University of California, Los Angeles, Los Angeles, CA, USA.
[8]These authors contributed equally: Zhaoqiang Wang, Ruixuan Zhao
[9]e-mail: gaol@g.ucla.edu

Abstract

Volumetric functional imaging of transient cellular signaling and motion dynamics poses a significant challenge to current microscopy techniques, primarily due to limitations in hardware bandwidth and the restricted photon budget within short exposure times. In response to this challenge, we present squeezed light field microscopy (SLIM), a computational imaging method that enables rapid detection of high-resolution three-dimensional (3D) light signals using only a single, low-format camera sensor area. SLIM pushes the boundaries of 3D optical microscopy, achieving over one thousand volumes per second across a large field of view of 550 μm in diameter and 300 μm in depth. Using SLIM, we demonstrated blood cell velocimetry across the embryonic zebrafish brain and in a free-moving tail exhibiting high-frequency swinging motion. The millisecond temporal resolution also enables accurate voltage imaging of neural membrane potentials in the leech ganglion. These results collectively establish SLIM as a versatile and robust imaging tool for high-speed microscopy applications.

Introduction

High-speed fluorescence microscopy has been playing an indispensable role in revealing the dynamic interplay and functionality among cells in their native environment. With continuous improvements in fluorescent markers, many transient biological processes, such as the blood flow[1] and neural action potentials[2–4], become trackable and, thus, demand microscopy with an ever higher spatiotemporal resolution. Traditional three-dimensional (3D) imaging tools, such

as confocal microscopy, light sheet microscopy, and two-photon microscopy, heavily rely on scanning to acquire a volumetric image. Despite advancement in beam shaping[5,6], remote refocusing mechanisms[7] and detection geometry[8], there persists an inherent trade-off between temporal resolution, the 3D field-of-view (FOV), and spatial resolution in these techniques. This constraint marks a significant challenge to obtain optimal performance across a large 3D field of view (FOV) for robust ultrafast detection exceeding kilohertz (kHz).

Computational imaging mitigates this trade-off by encoding high-dimensional information, such as depth[9], time[10], and spectra[11–13], into two-dimensional (2D) multiplexed camera measurements. Among these techniques, light-field microscopy (LFM) excelled in various biological applications, including observation of neural activity in freely moving animals[14–16] and visualization of hemodynamics in the brain[17] and heart[18–20]. By simultaneously collecting the spatial and angular information of light rays, LFM enables volumetric reconstruction *post hoc* from snapshot measurements. Without scanning, the sensor bandwidth becomes the primary bottleneck for LFM 3D imaging speed. While modern scientific Complementary Metal-Oxide Semiconductor (sCMOS) sensors typically offer a full framerate lower than 100 Hz, increasing the imaging speed can be achieved by reading out only selected low-format regions of interest (ROI). However, this approach comes at the cost of sacrificing either the spatial and/or angular components associated with the field of view (FOV) and axial resolution.

The integration of ultra-high-speed cameras[7,8,21] and event cameras[22] holds promise for providing higher bandwidths to LFM. However, their current limitations in sensitivity and noise performance present challenges, especially for photon-starved applications like imaging genetically encoded voltage indicators (GEVIs).[7] On the other hand, the compressibility of four-dimensional (4D) (two spatial dimensions plus two angular dimensions) light fields has been leveraged for compressive detection. Coded masks[23–25] and diffusers[26] are employed to modulate and integrate the spatio-angular components originally recorded by distinct pixels. Sparse nonlocal measurements can also be utilized across different angular views to acquire light fields with sensors of arbitrary formats.[27–29] Nevertheless, compressive imaging relies on sparsity priors and optimization algorithms for signal recovery from the sub-Nyquist measurement dataset. These methods are primarily validated on natural photographic scenes under ample lighting conditions. Their robustness and effectiveness in high-speed fluorescence microscopy remain elusive.

To address the unmet need for high-speed light-field imaging, we present herein Squeezed LIght field Microscopy (SLIM), which allows the capture of 3D fluorescent signals at kilohertz volume rates in a highly data-efficient manner. SLIM operates by acquiring an array of rotated 2D sub-aperture images. An anamorphic relay system applies anisotropic scaling, effectively 'squeezing' the image along one spatial axis. This allows the camera sensor to detect the light field using only a low-format letterbox-shaped ROI. Leveraging the row-by-row readout architecture of modern CMOS sensors, SLIM achieves a more than fivefold increase in acquisition rate compared to traditional LFM. Each squeezed sub-aperture image complements the others, facilitating high-fidelity 3D reconstruction from compressed measurement while preserving the nominal FOV and spatial resolution.

We demonstrated SLIM by capturing the flowing red blood cells in an embryonic zebrafish at 1,000 volumes per second (vps) and neural voltage spikes in leech ganglions at 800 vps. SLIM enables tracking high-speed cellular motion and millisecond membrane action potentials across a 550 µm FOV within a 300 µm depth range. Furthermore, we showcased that the high framerate of SLIM could be exploited to enhance axial resolution when combined with multi-layer scanning light-sheet microscopy. This allows for imaging densely labeled structures, previously challenging with LFM, such as contracting myocardium in a zebrafish, at 4,800 frames per second (fps), leading to a volume rate of 300 vps.

Results

Principle and design of SLIM

In a typical SLIM camera (**Fig. 1a**), the input scene is imaged by a combined system consisting of an array of dove prisms and lenslets (**Fig. 1ai**, **Supplementary Figure 1**). Each dove prism within the array is rotated at a distinct angle relative to its optical axis. This arrangement gives rise to an array of perspective images, each rotated at twice the angle of its corresponding dove prism's rotation, all converging at an intermediate image plane situated behind the lenslets. Subsequently, these rotated perspective images are further processed through an anamorphic relay system consisting of two cylindrical doublets with orthogonal optical axes (**Fig. 1aii**, **Supplementary Figures 2**). This relay system imparts anisotropic scaling to the image array, where the images experience de-magnification (0.2X) along one spatial axis while preserving the original magnification along the orthogonal direction. Finally, the rescaled image array is acquired by a 2D camera, where we read out only pixel rows that receive light signals (referred to as active readout ROI in **Fig. 1a**).

One of the key advantages of employing squeezed optical mapping is the improved readout speed. Modern CMOS sensors are equipped with parallel analog-to-digital converters (ADCs) for each column of pixels, ensuring consistent frame rates regardless of the number of pixel columns being readout. The frame rate is, therefore, solely determined by and inversely proportional to the number of pixel rows being readout. For example, on the Kinetix sCMOS developed by Teledyne, using an ROI of 200×3200 pixels allows SLIM to capture a 19 sub-aperture image array at 1,300 fps and 8,000 fps in 16-bit and 8-bit mode, respectively. In contrast, the full-frame mode achieves frame rates of only 83 fps (16-bit) and 500 fps (8-bit).

The forward model of SLIM is illustrated in **Fig. 1b**. Similar to Fourier LFM (FLFM)[15,30], SLIM can be conceptualized as a tomographic system, where each sub-aperture image is essentially a parallel projection of a 3D volume along a line of sight at the sub-aperture's view angle[31,32]. However, Unlike FLFM, where these sub-apertures images are directly captured by a 2D camera, SLIM applies in-plane rotation and vertical scaling operations to these images before recording.

In the 3D spatial frequency space, the Fourier spectrum of a SLIM sub-aperture image manifests as a 2D elliptical slice (Fourier Slice Theorem, **Supplementary Note 1**). The short axis of this ellipse corresponds to the low-resolution sampling along the squeezing direction. By using an array of sub-aperture images rotated at complementary angles, SLIM fills in the missing high-frequency information. This process results in a synthesized power spectrum with a bandwidth that approximates that of the original unsqueezed FLFM (**Fig. 1c**). In addition, the rotation angles of sub-aperture images are carefully crafted to maximize the horizontal projections of their 3D point spread functions (PSFs) (**Supplementary Figure 3**). In other words, when imaging a 3D object, the sub-aperture images of SLIM exhibit lateral disparity shifts due to their view angle difference. We optimize the rotation angle of each sub-aperture image to align its disparity shift with the unsqueezed spatial axis (*i.e.*, camera pixel row direction), thereby maximizing the samplings of disparity and consequently enhancing the axial resolution. This forward model can be further extended to wave optics by using a sum of 2D convolutions between the sample sliced at each depth and the corresponding sub-aperture PSF[15,30]. Through an iterative deconvolution algorithm, SLIM reconstructs the 3D fluorescence distribution by fusing all sub-aperture images (**Methods**).

We implemented selective volume illumination to suppress fluorescence outside the imaging volume (**Fig. 1d, Supplementary Figure 4**). Depending on the specific applications, we have the option to choose between two variants: 1. Scanning light sheet generated by a high-power laser source, capable of delivering up to 500 mW (**Fig. 1di**); 2. Static LED featuring ultra-low-noise performance (**Fig. 1dii**). The light sheet scanning is controlled by a galvo-mirror, and we synchronize the camera's exposure with a complete scan for synthetic volumetric illumination. On the other hand, we shape the LED's beam using a slit and project its conjugate image to the sample. The two methods share the same orthogonal illumination geometry.

Figure 1e-f show the 3D reconstruction of fluorescent beads of sub-diffraction size imaged by SLIM. At a magnification of 3.6X, the imaging volume spans a 3D space of $\emptyset 550\ \mu m \times 300\ \mu m$ with a spatial resolution of $3.6\ \mu m$ laterally and $6.0\ \mu m$ axially (**Supplementary Figures 3**). Despite a different sampling strategy, SLIM inherits the first-order parameters (*e.g.*, resolution, FOV, and depth range) of FLFM. More importantly, its highly efficient data acquisition manner alleviates the strain on the camera's bandwidth, thereby enabling kilohertz frame rates.

Imaging of flowing red blood cells in an embryonic zebrafish

Experimental characterization of blood flow in living organisms provides valuable insights into local metabolism, vascular development, and disease states. Using fluorescently labeled blood cells, various imaging methods have been demonstrated in single-cell velocimetry, such as in the larval zebrafish heart[8,19,33], tail[34,35], and mouse brain[1,17]. However, these methods are often limited to 2D imaging or restricted by a limited volumetric frame rate, which hinders the detection of fast flow and necessitates sedation of the animal to reduce motion artifacts. Here, we show that SLIM could be used to capture the fast-circulating red blood cells (RBCs) in a zebrafish at a kilohertz volumetric rate, both with and without anesthesia.

We imaged the transgenic zebrafish embryos expressing DsRed in RBCs at three days post fertilization (dpf). We excited the zebrafish brain using light-sheet-synthesized volumetric illumination and recorded fluorescence using SLIM with 19 sub-aperture images at 1,000 frames per second. The reconstruction reveals the 3D distribution of RBCs and allows for cell tracking over time (**Methods, Supplementary Figure 5**). **Figure 2a** shows two separate recordings from the dorsal and ventral view, each visualizing RBCs at representative time points (red) and the vasculature network by maximum intensity projection (MIP) throughout all frames (cyan). The flowing velocity is pulsatile temporally and varies spatially in the aorta and vein (**Supplementary Videos 1**). The tracking reveals the velocity distribution in 3D and highlights vessels with a high-speed flow of up to 6 mm/s (**Fig. 2a**). SLIM's kilohertz imaging seizes the transient motion at a millisecond time scale (**Fig. 2b**), effectively eliminating the motion blur and enabling robust cell tracking compared to a lower imaging rate (**Fig. 2c**).

We further demonstrated the speed advantage by imaging the free-moving tail of a zebrafish without anesthesia. The embryo was mounted on a cover glass with its head restrained using agarose while allowing the tail to move freely in the water. SLIM captured the high-frequency tail swings without any motion blur (**Fig. 2d, Supplementary Videos 2**), maintaining its capability to track individual RBCs and revealing the compound movement that combines oscillation vertical to the tail plane and normal progression along the vessels (**Fig. 2e**). By combining with closed-loop tracking and a translational stage[15], SLIM's high-speed volumetric imaging holds promise for studying hemodynamics under natural conditions during locomotor behavior.

Optical recording of membrane action potentials in medicinal leech ganglions

The development of voltage imaging has enabled neuroscientists to examine neural dynamics with a high spatio-temporal resolution. However, it has long been a challenge to capture voltage signals *in vivo* across a large volume due to the extremely fast transients and low signal-to-noise ratio. With its millisecond temporal resolution, SLIM can precisely detect spike timings across a large 3D neural network, opening avenues for mapping the intricate interaction of neuronal components and elucidating the mechanisms underlying sensory processing and behavioral generation.

As a demonstration, we loaded a voltage-sensitive dye (FluoVolt, F10488, Thermo Fisher Scientific) to a dissected ganglion from a medicinal leech.[36] Using SLIM, we recorded the fluorescent signals with 29 sub-aperture images at 800 Hz under the illumination of an ultra-low-noise LED. Concurrently, we introduced a microelectrode for simultaneous electrophysiological stimulation and recording (**Fig. 3a**). Timing and waveforms (**Fig. 3b**) of neuronal action potentials are adequately sampled from the reconstructed 3D image sequence (**Fig. 3c, Supplementary Videos 3**). We further processed the data by manually choosing an area of interest on each cell, averaging pixels from the corresponding cell membrane, and correcting motion drift (**Methods, Supplementary Figure 6,7**). The resultant time-lapse fluorescence intensities at selected neurons are shown in **Fig.3d**. SLIM measurements agreed

with the electrophysiological record in quantitative detail, including the reduction of spike amplitude while strong depolarizing currents were applied.

Imaging of free-swimming *Vibrio cholerae* bacteria

Bacterial chemotaxis is a behavior in which cells sense and respond to chemical gradients in order to swim using their flagellar appendages towards favorable chemoattractants and avoid harmful substances.[37,38] Chemotaxis and flagellar swimming motility are important components of virulence pathways and bacterial pathogenicity.[39] Fully capturing this behavior in 3D, however, is difficult due to the high swimming speeds of the cells and the 3D nature of their trajectories. The current standard for imaging bacterial swimming involves a computational approach by matching diffraction patterns in a 2D image to a reference library in order to reconstruct the 3D positional information of the cell for tracking.[40] A major limitation of this technique is the imaging rate, which is typically around 10-30Hz. For a swimming bacterium (*Vibrio cholera* average swim speeds are around 100 µm/s), this imaging rate will result in about 5-10 µm of displacement between sequential images. Since this displacement is several cell body lengths long, much of the detailed behavior will not be captured.

To demonstrate SLIM's capability in addressing this challenge, we imaged the dynamic behaviors of swimming *Vibrio cholerae*. Our setup involved capturing 29 sub-aperture images at a rate of 200 frames per second, facilitated by light-sheet-synthesized volumetric illumination (**Fig. 4a**). This allows us to track each individual bacterium within imaging space simultaneously (**Fig. 4b**) and obtain information about its swimming trajectory (**Fig. 4c**) by MIP throughout all frames. This higher imaging volume rate reduces the spatial displacement in a cell's trajectory between sequential images allowing for observation of finer details in swimming behaviors, such as reversal events occurring during the "run-reverse-flick" behavior in *Vibrio cholera* (first picture of **Fig. 4d,** also shown in **Supplementary Videos 4**), where the change in flagellar rotation direction causes a buckling and subsequent reorientation of the swimming direction out of the conventional 2D plane of imaging.[41] The high volumetric imaging speed also allows us to quantify the diffusivity of swimming cells by calculating the Mean Squared Displacement (MSD) slope and Radius of Gyration of their trajectories, as labeled in **Fig. 4d**[42], a task that is typically challenging with conventional 3D microscopy techniques.

Imaging of a beating embryonic zebrafish heart with scanning multi-sheet illumination

Although LFM techniques, including SLIM, offer the ability to numerically refocus to specific depths, they typically lack intrinsic optical sectioning capability. Its application is potentially hindered by the spatial resolution and reconstruction artifacts, and it favors objects with high sparseness.[43] Here, we demonstrated that SLIM can be combined with scanning multi-sheet illumination. The synergy enables high-contrast 3D imaging of densely-labeled fluorescent objects.

We constructed a dual-light-sheet illumination module and scanned the beams using a galvo-mirror driven by a sawtooth function. Rather than synchronizing the camera exposure with the entire scan range as in previous experiments, we operated the camera at a higher rate, allowing each frame to capture a subset of depth layers of the fluorescent object (**Fig. 5a**). This approach significantly suppresses out-of-focus light and improves axial resolution in the reconstruction, as shown on fluorescent beads and zebrafish vasculature networks (*Tg*(flk:mCherry)) (**Fig. 5b,c, Supplementary Videos 5**). On the other hand, SLIM offers an ultra-high framerate and supports simultaneous multi-plane detection. These features enable SLIM to maintain a high volume rate even within this scanning scheme.

We demonstrated this acquisition scheme by imaging a beating zebrafish heart (*Tg*(cmlc2:GFP)) at 300 vps (**Fig. 5d, Supplementary Videos 6**). This is achieved by scanning the dual light sheets at 300 Hz, synchronized with camera recording at 4,800 fps (8-bit speed mode, see **Methods**). This setup allowed us to reconstruct the heart with 30 planes across 200 μm depth range with the microstructures like ventricular trabeculation clearly delineated (**Fig. 5d,e**). The enhanced spatial resolution and contrast offer the potential for accurate segmentation of the heart chamber's geometry, facilitating cardiac studies, such as regional myocardial contractility analysis[33] and computational fluid dynamics (CFD) for hemodynamic forces simulation[44]. While current LFM cardiac imaging is mostly demonstrated on sparse markers like cardiomyocyte nuclei[18,19,45] and blood cells[19,20,46], SLIM with scanning multi-sheet illumination proves effective in resolving the densely labeled muscle tissue. It provides high 3D imaging speed to capture the beating heart in real time and outlines the time-dependent chamber dimension to detect beat-to-beat variations (**Fig. 5f**).

Discussion

We presented SLIM as an innovative snapshot 3D detection method that addresses the pressing need for high-speed volumetric microscopy operating at kilohertz speeds. SLIM accomplishes this by capturing a condensed representation of the original light field using a compact ROI on the sensor. The sampling strategy is grounded in the principle that the inherent spatio-angular correlation in the light field can be exploited to recover signals from compressive measurement.[23,27] Validations across a range of applications, including hemodynamics, neural imaging, cardiovascular imaging, and bacterial dynamics, demonstrated SLIM's versatility and robustness.

SLIM's kilohertz 3D imaging speed, rarely provided by existing methods and often entailing significant design tradeoffs and demanding hardware requirements[22,47], presents new opportunities to investigate millisecond-scale dynamics in emerging fields like voltage imaging. It is universally adaptable to the vast majority of CMOS sensors, which generally allow higher frame rates at reduced readout pixel rows. While we set kilohertz as a milestone for 3D fluorescence microscopy, SLIM has the potential to achieve tens and even hundreds of

thousands of vps with current high-speed cameras[48]. It mitigates the trade-off between speed and other sensor characteristics, allowing us to prioritize cameras with higher sensitivity, lower noise, or other favorable attributes. It also presents great potential in imaging applications where limitations exist on camera pixel count due to fabrication complexity and cost, such as fluorescence lifetime imaging microscopy[49] and short-wave-infrared imaging[50].

SLIM offers a snapshot acquisition that effectively addresses the trade-off between pixel exposure time and volumetric frame rate encountered in conventional scanning-based 3D optical microscopy techniques. This unique approach gives SLIM distinct advantages in terms of photon efficiency and signal-to-noise ratio (SNR), especially beneficial for high-speed imaging of weak fluorescence.

The in-plane rotations and anisotropic scaling in SLIM are co-designed for reconstructing a FOV with a higher resolution than that of each sub-aperture image. This design is specifically tailored to utilize a low-format rectangular sensor, marking a fundamental departure from existing compressive light field photography.[23–25] The latter, stemming from coded aperture imaging, retrieves light fields at the same or lower resolutions than the multiplexed measurement. Moreover, SLIM does not require multiple shots[23] or learning on a sparse basis prior to reconstruction[25]. Our algorithm also bypasses the computational complexity associated with solving the 4D light field and directly reconstructs the 3D image stack for microscopy applications.

SLIM inherits the first-order parameters from FLFM, including magnification, numerical aperture (NA), and FOV. It can transform an existing FLFM[15,30,43,51] into a high-speed 3D imager with a significantly higher frame rate. However, like FLFM, SLIM faces challenges such as compromised spatial resolution, depth-variant performance, and limited considerations for tissue scattering and lens aberrations. These factors constrain its applicability in complicated intravital environments. We have shown that multi-sheet scanning can extend SLIM's capability to densely-labeled tissue imaging. The refocusing capability within a largely extended depth of field makes SLIM compatible with various 3D illumination structures. Additionally, the literature presents several strategies to enhance SLIM's performance, such as background rejection by hardware[17] and computation[52], multi-focus optics for extended DoF[15,53], and sparsity-based resolution enhancement[43,54]. Furthermore, ongoing advancements in data-driven reconstruction algorithms, particularly physics-embedded deep learning models[19,20,45,55], hold great promise for addressing the ill-posed inverse problems associated with limited space-bandwidth and compressive detection in SLIM. These developments are expected to significantly enhance SLIM's capabilities and broaden its utility across diverse imaging scenarios.

Acknowledgements

We would like to thank Y. Dong, Y. Zhang, and J. Wang at UCLA for their assistance in zebrafish experiments. We acknowledge the David Geffen School of Medicine at UCLA for providing the Zebrafish Core Facilities. This work was supported by the following grants: National Institutes of

Health (NIH) (R01HL165318, 2R01GM067180, RF1NS128488). W.C.S. was supported by NSF Graduate Research Fellowship Program (DGE-1650604, DGE-2034835) and Ruth L. Kirschstein National Research Service Award "Multidisciplinary Training in Microbial Pathogenesis" (T32AI007323).

Author contributions

Z.W. and L.G. conceived the idea. L.G., D.A.W., R.L., G.C.W and T.K.H. oversaw the project. Z.W. designed and constructed the optical setups. Z.W. developed the reconstruction algorithm. W.K. fabricated the lenslet array. Z.W., R.Z., D.A.W., C.K.L., W.C.S., A.P., and E.Z. prepared the samples and Z.W., R.Z., D.A.W., A.P., and E.Z. performed the imaging experiments. Z.W. and R.Z. processed and analyzed the data. Z.W., R.Z., and L.G. wrote and prepared the manuscript. All authors reviewed, edited, and consulted on the manuscript text.

Competing interests

Liang Gao has a financial interest in Lift Photonics. However, it was not involved in the research presented in this paper.

Methods

Hardware setup

We built a light field microscope employing selective volume illumination. The detection setup features a 20X water-dipping objective (N20X-PFH, Olympus XLUMPLFLN 20X, 1.0 NA). A 4F relay system (AC508-180-A, AC508-200-A, Thorlabs) forms a conjugate plane of the objective's back pupil, accommodating a customized dove prism and a spherical lenslet array. The dove prism (aperture length: 1.3 mm, material: H-K9L, fabricated by Changchun Sunday Optics) is positioned anteriorly to the plano-convex lenslet (aperture diameter: 1.3 mm, focal length: 36 mm, material: PMMA, fabricated in-house). Each pair generates a rotated sub-aperture image with a magnification of 3.6X and NA of 0.065. In total, 29 pairs are utilized and securely housed in 3D-printed mechanical holders (refer to **Supplementary Figure 1** for detailed designs of the prism, lenslet, and holder). Our anamorphic relay system comprises a spherical achromat doublet (ACT508-250-A, Thorlabs) and two orthogonally oriented cylindrical achromat doublets (ACY254-250-A, ACY254-50-A, Thorlabs). The back focal planes of two cylindrical lenses are co-located, producing an image with an anisotropic scaling factor (**Supplementary Figure 2**). A sCMOS camera (Kinetix, Teledyne) captures the final image, with a $320 \times 3200\ px$ ROI covering all 29 sub-aperture images, or a $200 \times 3200\ px$ ROI for 19 sub-aperture images. The maximal readout speeds for two ROIs are 830 fps and 1,328 fps in 16-bit dynamic range mode and 5,000 fps and 8,000 fps in 8-bit speed mode. The 29 sub-aperture configuration collects around 50% more light than the 19 sub-aperture one.

The illumination sources include blue and green continuous lasers (MBL-FN-473-500mW and MGL-III-532-300mW, CNI Laser) and an ultra-low-noise blue LED (UHP-T-470SR Prizmatix). For scanning light sheet setup, we use a knife-edge mirror (MRAK25-G01, Thorlabs) to combine two beams with adjustable spacing and a galvo-mirror (GVS011, Thorlabs) to scan them together. Planar illumination is formed perpendicular to the detection axis by a cylindrical lens and a dry objective (RMS4X-PF, Olympus 4X, 0.13 NA). We use a sawtooth function to drive the galvo-mirror. In synthetic volume illumination configuration, we block one light sheet beam. The camera is then triggered at the beginning of the sawtooth waveform and exposed for the entire scan. In scanning plane illumination configuration, we use two light sheet beams and trigger the camera multiple times during a scan. The static LED setup shares the same illumination objective and perpendicular geometry. We built a Koehler illumination system and used an adjustable slit as a field aperture. The conjugate image of the slit is relayed to the sample, and the slit controls the depth range of the beam. The LED provides ultra-stable illumination power and thus suppresses excitation source noise during our voltage imaging experiments. See Supplementary Figure 3 for system schematics and **Supplementary Table 1** for hardware configurations used in different experiments.

Image formation and reconstruction

The light field of the fluorescent sample is acquired by dividing the objective's back pupil with a lenslet array and recording a group of sub-aperture images. Depending on their sub-aperture locations, they display disparity, that is the distinct displacement shown by the same signal. After calibrating the displacement at every axial position, the formation of each sub-aperture image can be modeled as a sum of laterally shifted depth slices. We replace the shifting operator with a convolution with PSF to account for both the diffraction and displacement. A dove prism is a truncated right-angle prism and used to rotate the incident beam. The rotation of the prism around its longitudinal axis causes the beam to rotate at twice the rate of the prism's rotation. By placing a dove prism array in the infinity space between the objective and lenslet array, we apply varying in-plane rotations to sub-aperture images. Finally, we adopt an anamorphic relay system to introduce anisotropic scaling to the image array: we de-magnify (squeeze) the image in the direction perpendicular to the camera read-out axis while maintaining the original scale in the other direction (**Supplementary Figure 2**). This one-axis scaling and the aforementioned in-plane rotation are both directly applied to the 3D fluorescent image in our model.

Given a 3D fluorescence distribution $O(x, y, z)$ and system PSF, the formation of camera measurement $I(x, y, v)$ can be modeled as:

$$I(x, y, v) = \sum_{z} (S \cdot R(v) \cdot O(x, y, z)) \otimes PSF(x, y, z, v), \qquad (1)$$

where v is the index of sub-aperture, $\otimes$ represents the 2D convolution, $R(v)$ applies sub-aperture-dependent rotation from the dove prism, and S introduces image scaling from the anamorphic relay system.

The volume reconstruction algorithm was derived from Richardson-Lucy deconvolution[56]. Based on the forward model (1), the 3D fluorescence distribution $O(x, y, z)$ is iteratively solved from the camera measurements $I(x, y, v)$ and empirical point spread functions PSF (**Supplementary Software**).

The rotation angles and image scaling factor are pre-calibrated as known priors in the reconstruction. The measurement patch $I(x, y, v)$ is cropped from the raw sensor image according to the center location of each sub-aperture image. We measure the point spread functions by scanning a sub-diffraction fluorescent bead at different axial positions using a motorized translation stage. The PSF is assumed to be spatially invariant within each sub-aperture image.

With our implementation, each measurement patch $I(x, y, v)$ has a resolution of 301×61 px. The numbers of channels (v) and axial slices (z) are configured based on the targeted framerate and depth range/step size. For example, with 19 sub-aperture measurements to reconstruct a volume of $305 \times 305 \times 151$ px, the deconvolution takes around 30 seconds via eight iterations using a desktop computer with a modest GPU (Nvidia RTX 3070).

Fluorescent beads imaging and resolution characterization

Fluorescent microspheres of 1 um (F13082, ThermoFisher) were embedded in 1% low-melting agarose and injected into a transparent fluorinated ethylene propylene tube for imaging. To acquire experimental PSFs, the solution was highly diluted to keep only one bead in the FOV. For spatial resolution quantification, the beads were randomly distributed in space, and we measured the full width at half maximum (FWHM) of the bead image at various locations in the FOV (**Supplementary Figure 3**). We also performed two-point resolving experiments by reconstructing synthetic measurements that added two sequentially captured frames. We translated the bead laterally and axially at varying distances in these two frames. The resolution was then indicated by the resolvable set with the least distance (**Supplementary Figure 3**).

Fish husbandry and imaging

Transgenic zebrafish lines *Tg*(gata1a:dsRed), *Tg*(flk:mCherry), and *Tg*(cmlc:GFP) were used in our experiments for imaging blood cells, endothelial cells, and myocardium, respectively. Embryonic fish were maintained at three days post-fertilization in standard E3 medium, which was supplemented with extra 1-phenyl 2-thiourea (Sigma Aldrich) to inhibit melanogenesis at day one. For brain hemodynamics and cardiac imaging, the larvae were anesthetized with tricaine (3-aminobenzoic acid ethyl ester, Sigma Aldrich) and immobilized in 1% low-melting-point agarose inside a fluorinated ethylene propylene tube before imaging. For tail experiments, the larvae were first positioned on cover glass before the heads were fixed by 3% low-melting-point agarose. Immediately after the agarose solidified, the sample was immersed in a water chamber. The imaging starts after visually confirming the unconstrained movement of the tail.

All the experiments were performed in compliance with and with the approval of a UCLA IACUC protocol.

Blood cell velocimetry

3D cell tracking was performed by ImageJ and the plugin Trackmate[57,58]. We used the DoG (Difference of Gaussian) blob detector and the LAP (linear assignment problem) tracker for all experiments. The spot positions and trajectory properties were exported to MATLAB for further analysis and visualization. We removed the local oscillation from the tracking result by fitting a center line of each trajectory with a smooth spline. The tangential velocity was calculated by projecting the cell displacement in adjacent frames onto the center line. The trajectories were then color-coded by the tangential velocity to display the blood flow speed along the vessels. The tracking accuracy (**Supplementary Figure 5**)

Leech sample preparation

Medicinal leeches (*Hirudo verbana*) obtained from leech.com were housed in artificial pond water maintained at 15°C. Detailed dissection procedures have been described before.[36,59] Briefly, an adult leech was anesthetized in ice-cold leech saline and an individual segmental ganglion (M10) was dissected out. The ganglion was pinned down ventral side up on a rectangular-shaped flat substrate made of Polydimethylsiloxane (PDMS) (Sylgard 184, Dow Corning). After removing the sheath that covers the ganglion, a voltage-sensitive dye[60] (FluoVolt, ThermoFisher) was bath-loaded using a peristaltic pump. The sample was placed under the detection objective of the SLIM system for imaging.

Leech ganglion electrophysiology and imaging

Glass microelectrodes (20–50 MΩ) were filled with a recording solution of 3 M potassium acetate and 60 mM potassium chloride. After penetrating the membrane of a cell of interest, small negative holding currents were injected to ensure stability. All electrophysiology used Neuroprobe amplifiers (Model 1600; A-M systems). Membrane voltage and electrode current were digitized along with the camera trigger signal at 10 kHz using a 16-bit data acquisition board (NI USB-6002; National Instruments). We used the camera triggers as time stamps to align recorded frames with electrophysiological data.

After image reconstruction, we corrected for sample movement by running a 2D registration and demotion between adjacent frames using a modified version of SWiFT-IR[61]. The 3D ROIs were then manually defined for each neuron. And the optical readout F_t was calculated by averaging the pixel intensities in the ROI and normalized by the temporal baseline: $F = (F_t - F_0)/F_0$, where F_0 is the temporal mean value. To detect spikes from the optical signal, we detrended the trace F by subtracting its median-filtered version (window size, 50 ms). It was

then binarized by a Schmitt trigger, and a peak detection was performed to locate the voltage spikes.

Vibrio cholerae Strain and Preparation Conditions

Wild Type Vibrio cholerae O1 El Tor strain A1552 were grown in lysogeny broth (LB) at 30°C with 200rpm shaking for 22 hours to stationary phase. Cell cultures were then diluted 1:1000 in 1mL of 2% LB media pre-mixed with 0.1ug/mL FM1-43FX membrane stain (Life Technologies F35355). 50uL of the stained cell culture was then loaded into a transparent FEP tube and sealed for imaging.

Vibrio cholerae swimming metrics

The Radius of Gyration(RoG) quantifies the average movement of a trajectory over time which is defined as: $RoG = \sqrt{\sum_{k=1}^{N} |r_k - r_{mean}|^2 / N}$, where r_k is the kth position of the cell, r_{mean} is the mean position and N is the total number of tracking point. Another metrics we used for quantifying the diffusivity of a trajectory is Mean Square Displacement slope (MSD slope) which is a commonly used metric in colloidal studies and biophysics to determine what is the mode of displacement of particles followed over time. We used Msdanalyzer[62] for MSD slope calculation for all trajectories (https://github.com/tinevez/msdanalyzer).

Image reconstruction with scanning multi-plane illumination

The axial positions of plane illumination during a scan were calibrated using fluorescent beads. For each scanning step, we reconstructed the bead measurement and localized two slices exhibiting the highest image contrasts. In the following imaging experiments, the same slices were sampled from the reconstruction and constituted a new stack with all other scanning steps. During high-speed scans, the sawtooth function that drives the galvo mirror could suffer from the limited bandwidth of the waveform generator. We removed the measurements at the beginning/end of the scan if repeating abnormalities (that happened at every cycle) were observed during the calibration. For image reconstruction of each scanning step, we treated it as the same reconstruction problem under volumetric illumination.

Data availability

The data generated and analyzed in this study are available from the corresponding author upon request.

Code availability

Codes for 3D reconstruction can be found in Supplementary Software.

Reference

1. Meng, G. *et al.* Ultrafast two-photon fluorescence imaging of cerebral blood circulation in the mouse brain in vivo. *Proceedings of the National Academy of Sciences* **119**, e2117346119 (2022).
2. Abdelfattah, A. S. *et al.* Bright and photostable chemigenetic indicators for extended in vivo voltage imaging. *Science* **365**, 699–704 (2019).
3. Abdelfattah, A. S. *et al.* Sensitivity optimization of a rhodopsin-based fluorescent voltage indicator. *Neuron* **111**, 1547-1563.e9 (2023).
4. Hochbaum, D. R. *et al.* All-optical electrophysiology in mammalian neurons using engineered microbial rhodopsins. *Nat Methods* **11**, 825–833 (2014).
5. Wu, J. *et al.* Kilohertz two-photon fluorescence microscopy imaging of neural activity in vivo. *Nat Methods* **17**, 287–290 (2020).
6. Zhang, T. *et al.* Kilohertz two-photon brain imaging in awake mice. *Nat Methods* **16**, 1119–1122 (2019).
7. Wang, Z. *et al.* Imaging the voltage of neurons distributed across entire brains of larval zebrafish. 2023.12.15.571964 Preprint at https://doi.org/10.1101/2023.12.15.571964 (2023).
8. Voleti, V. *et al.* Real-time volumetric microscopy of in vivo dynamics and large-scale samples with SCAPE 2.0. *Nat Methods* **16**, 1054–1062 (2019).
9. Pavani, S. R. P. *et al.* Three-dimensional, single-molecule fluorescence imaging beyond the diffraction limit by using a double-helix point spread function. *Proceedings of the National Academy of Sciences* **106**, 2995–2999 (2009).

10. Llull, P. *et al.* Coded aperture compressive temporal imaging. *Opt. Express, OE* **21**, 10526–10545 (2013).

11. Wagadarikar, A. A., Pitsianis, N. P., Sun, X. & Brady, D. J. Video rate spectral imaging using a coded aperture snapshot spectral imager. *Opt. Express, OE* **17**, 6368–6388 (2009).

12. Zhao, R., Cui, Q., Wang, Z. & Gao, L. Coded aperture snapshot hyperspectral light field tomography. *Opt. Express, OE* **31**, 37336–37347 (2023).

13. Cui, Q., Park, J., Ma, Y. & Gao, L. Snapshot hyperspectral light field tomography. *Optica, OPTICA* **8**, 1552–1558 (2021).

14. Prevedel, R. *et al.* Simultaneous whole-animal 3D imaging of neuronal activity using light-field microscopy. *Nat Methods* **11**, 727–730 (2014).

15. Cong, L. *et al.* Rapid whole brain imaging of neural activity in freely behaving larval zebrafish (Danio rerio). *eLife* **6**, e28158 (2017).

16. Skocek, O. *et al.* High-speed volumetric imaging of neuronal activity in freely moving rodents. *Nat Methods* **15**, 429–432 (2018).

17. Zhang, Z. *et al.* Imaging volumetric dynamics at high speed in mouse and zebrafish brain with confocal light field microscopy. *Nat Biotechnol* **39**, 74–83 (2021).

18. Wagner, N. *et al.* Instantaneous isotropic volumetric imaging of fast biological processes. *Nat Methods* **16**, 497–500 (2019).

19. Wang, Z. *et al.* Real-time volumetric reconstruction of biological dynamics with light-field microscopy and deep learning. *Nat Methods* **18**, 551–556 (2021).

20. Lu, Z. *et al.* Virtual-scanning light-field microscopy for robust snapshot high-resolution volumetric imaging. *Nat Methods* **20**, 735–746 (2023).

21. Tian, T., Yuan, Y., Mitra, S., Gyongy, I. & Nolan, M. F. Single Photon Kilohertz Frame Rate Imaging of Neural Activity. *Advanced Science* **9**, 2203018 (2022).

22. Guo, R. *et al.* EventLFM: Event Camera integrated Fourier Light Field Microscopy for Ultrafast 3D imaging. Preprint at https://doi.org/10.48550/arXiv.2310.00730 (2023).

23. Ashok, A. & Neifeld, M. A. Compressive light field imaging. in *Three-Dimensional Imaging, Visualization, and Display 2010 and Display Technologies and Applications for Defense, Security, and Avionics IV* vol. 7690 221–232 (SPIE, 2010).

24. Babacan, S. D. *et al.* Compressive Light Field Sensing. *IEEE Transactions on Image Processing* **21**, 4746–4757 (2012).

25. Marwah, K., Wetzstein, G., Bando, Y. & Raskar, R. Compressive light field photography using overcomplete dictionaries and optimized projections. *ACM Trans. Graph.* **32**, 46:1-46:12 (2013).

26. Antipa, N., Necula, S., Ng, R. & Waller, L. Single-shot diffuser-encoded light field imaging. in *2016 IEEE International Conference on Computational Photography (ICCP)* 1–11 (2016). doi:10.1109/ICCPHOT.2016.7492880.

27. Feng, X., Ma, Y. & Gao, L. Compact light field photography towards versatile three-dimensional vision. *Nat Commun* **13**, 3333 (2022).

28. Feng, X. & Gao, L. Ultrafast light field tomography for snapshot transient and non-line-of-sight imaging. *Nat Commun* **12**, 2179 (2021).

29. Wang, Z., Hsiai, T. K. & Gao, L. Augmented light field tomography through parallel spectral encoding. *Optica, OPTICA* **10**, 62–65 (2023).

30. Guo, C. *et al.* Fourier light-field microscopy. *Opt. Express, OE* **27**, 25573–25594 (2019).

31. Levoy, M., Ng, R., Adams, A., Footer, M. & Horowitz, M. Light field microscopy. *ACM Trans. Graph.* **25**, 924–934 (2006).

32. Broxton, M. *et al.* Wave optics theory and 3-D deconvolution for the light field microscope. *Opt. Express, OE* **21**, 25418–25439 (2013).

33. Wang, Z. *et al.* A hybrid of light-field and light-sheet imaging to study myocardial function and intracardiac blood flow during zebrafish development. *PLOS Computational Biology* **17**, e1009175 (2021).

34. Roustaei, M. *et al.* Computational simulations of the 4D micro-circulatory network in zebrafish tail amputation and regeneration. *Journal of The Royal Society Interface* **19**, 20210898 (2022).

35. Zhou, Y., Zickus, V., Zammit, P., Taylor, J. M. & Harvey, A. R. High-speed extended-volume blood flow measurement using engineered point-spread function. *Biomed. Opt. Express, BOE* **9**, 6444–6454 (2018).

36. Tomina, Y. & Wagenaar, D. A. A double-sided microscope to realize whole-ganglion imaging of membrane potential in the medicinal leech. *eLife* **6**, e29839 (2017).

37. Berg, H. C. Chemotaxis in Bacteria. *Annual Review of Biophysics* **4**, 119–136 (1975).

38. Keegstra, J. M., Carrara, F. & Stocker, R. The ecological roles of bacterial chemotaxis. *Nat Rev Microbiol* **20**, 491–504 (2022).

39. Butler, S. M. & Camilli, A. Going against the grain: chemotaxis and infection in Vibrio cholerae. *Nat Rev Microbiol* **3**, 611–620 (2005).

40. Grognot, M., Mittal, A., Mah'moud, M. & Taute, K. M. Vibrio cholerae Motility in Aquatic and Mucus-Mimicking Environments. *Applied and Environmental Microbiology* **87**, e01293-21 (2021).

41. Son, K., Guasto, J. S. & Stocker, R. Bacteria can exploit a flagellar buckling instability to change direction. *Nature Phys* **9**, 494–498 (2013).

42. Conrad, J. C. *et al.* Flagella and Pili-Mediated Near-Surface Single-Cell Motility Mechanisms in *P. aeruginosa*. *Biophysical Journal* **100**, 1608–1616 (2011).

43. Yoon, Y.-G. *et al.* Sparse decomposition light-field microscopy for high speed imaging of neuronal activity. *Optica, OPTICA* **7**, 1457–1468 (2020).

44. Vedula, V. *et al.* A method to quantify mechanobiologic forces during zebrafish cardiac development using 4-D light sheet imaging and computational modeling. *PLOS Computational Biology* **13**, e1005828 (2017).

45. Wagner, N. *et al.* Deep learning-enhanced light-field imaging with continuous validation. *Nat Methods* **18**, 557–563 (2021).

46. Zhang, Y. *et al.* DiLFM: an artifact-suppressed and noise-robust light-field microscopy through dictionary learning. *Light Sci Appl* **10**, 152 (2021).

47. Sacconi, L. *et al.* KHz-rate volumetric voltage imaging of the whole Zebrafish heart. *Biophysical Reports* **2**, 100046 (2022).

48. HiCAM: High-Speed, High-Sensitivity Imaging Camera - Lambert. *lambertinstruments.com* https://lambertinstruments.com/products/hicam (2020).

49. Datta, R., Heaster, T. M., Sharick, J. T., Gillette, A. A. & Skala, M. C. Fluorescence lifetime imaging microscopy: fundamentals and advances in instrumentation, analysis, and applications. *JBO* **25**, 071203 (2020).

50. Wang, F. *et al.* Light-sheet microscopy in the near-infrared II window. *Nat Methods* **16**, 545–552 (2019).

51. Yi, C. *et al.* Video-rate 3D imaging of living cells using Fourier view-channel-depth light field microscopy. *Commun Biol* **6**, 1–8 (2023).

52. Zhang, Y. *et al.* Computational optical sectioning with an incoherent multiscale scattering model for light-field microscopy. *Nat Commun* **12**, 6391 (2021).

53. Zhang, Y. *et al.* Multi-focus light-field microscopy for high-speed large-volume imaging. *PhotoniX* **3**, 30 (2022).

54. Pégard, N. C. *et al.* Compressive light-field microscopy for 3D neural activity recording. *Optica, OPTICA* **3**, 517–524 (2016).

55. Zhu, L. *et al.* Sustained 3D isotropic imaging of subcellular dynamics using adaptive VCD light-field microscopy 2.0. 2023.03.15.532876 Preprint at https://doi.org/10.1101/2023.03.15.532876 (2023).

56. Biggs, D. S. C. & Andrews, M. Acceleration of iterative image restoration algorithms. *Appl. Opt., AO* **36**, 1766–1775 (1997).

57. Ershov, D. *et al.* TrackMate 7: integrating state-of-the-art segmentation algorithms into tracking pipelines. *Nat Methods* **19**, 829–832 (2022).

58. Tinevez, J.-Y. *et al.* TrackMate: An open and extensible platform for single-particle tracking. *Methods* **115**, 80–90 (2017).

59. Tomina, Y. & Wagenaar, D. Dual-sided Voltage-sensitive Dye Imaging of Leech Ganglia. *BIO-PROTOCOL* **8**, (2018).

60. Miller, E. W. *et al.* Optically monitoring voltage in neurons by photo-induced electron transfer through molecular wires. *Proceedings of the National Academy of Sciences* **109**, 2114–2119 (2012).

61. Wetzel, A. W. *et al.* Registering large volume serial-section electron microscopy image sets for neural circuit reconstruction using FFT signal whitening. in *2016 IEEE Applied Imagery Pattern Recognition Workshop (AIPR)* 1–10 (2016). doi:10.1109/AIPR.2016.8010595.

62. Tarantino, N. *et al.* TNF and IL-1 exhibit distinct ubiquitin requirements for inducing NEMO–IKK supramolecular structures. *Journal of Cell Biology* **204**, 231–245 (2014).

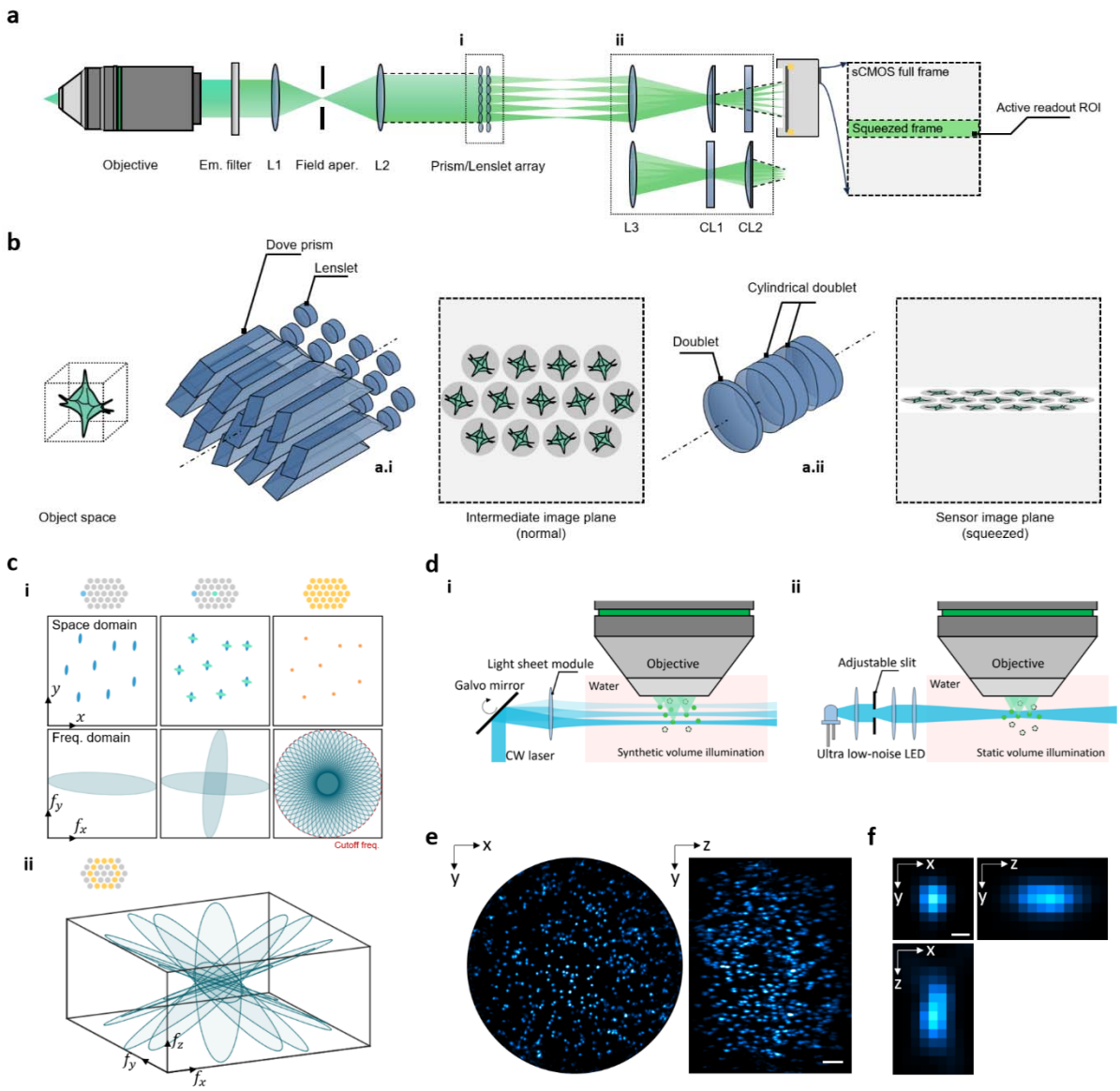

Fig. 1. Principle of SLIM. a. Schematic of SLIM detection system. L1-L3, achromatic doublet. CL1-CL2, achromatic cylindrical doublet. SLIM records light field at kilohertz frame rates by using a reduced active readout ROI on the camera. **b.** The optical transformation in SLIM comprises image rotation and squeezing, performed by a dove prism/lenslet array (**a.i**) and a customized anamorphic relay (**a.ii**). **c.** (i) Each sub-aperture, after reversing the squeezing and rotation, gives an image with anisotropic spatial resolution but complementary to others. By merging different sub-aperture images, SLIM estimates the original features. (ii) Transfer functions of SLIM by analyzing sub-aperture images as geometrical projections. Each gives an elliptical slice in the 3D frequency space, depending on its rotation angle and sub-aperture location. **d.** Selective volume illumination with a scanning light sheet (i) and LED (ii). **e.** 3D MIPs of fluorescent beads. Scale bar, 50 μm. **f.** Cross-sections of single bead showing representative PSFs. Scale bar, 3 μm.

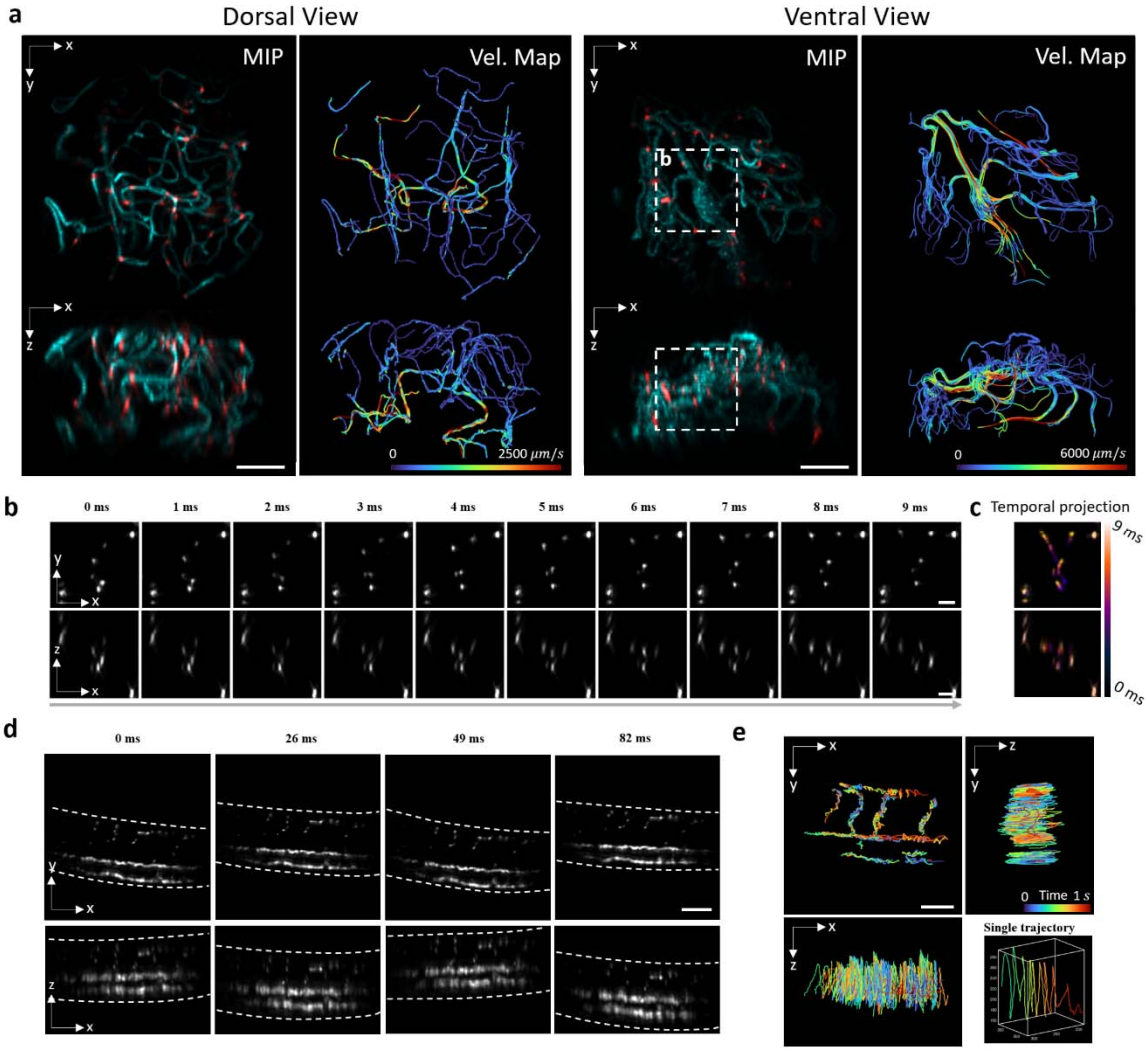

Fig. 2. 3D imaging of hemodynamics in the embryonic zebrafish brain and tail at 1,000 vps. a. MIPs of flowing blood cells at representative time points (red) and vascular network obtained by combining frames over time (cyan). The velocity maps show overlaid RBC trajectories color-coded by their instantaneous velocity. Two views, the dorsal view, and ventral view, are two datasets taken with differently-orientated embryos. Scale bar, 100 μm. **b.** Zoom-in time-lapse of the region labeled by the white dotted box in **a**. Scale bar, 30 μm. **c.** Temporal projection color-coded by the time visualizes the motion blur with a lower imaging speed. **d.** MIPs of a free-moving fish tail. **e.** RBC trajectories from **d** are color-coded by time. The coordinate system has been rotated so that the x-y plane shows the RBC movement perpendicular to the tail swing direction. The single trajectory on the bottom right exhibits the compound motion of a single RBC during fish swimming. Scale bar, 100 μm.

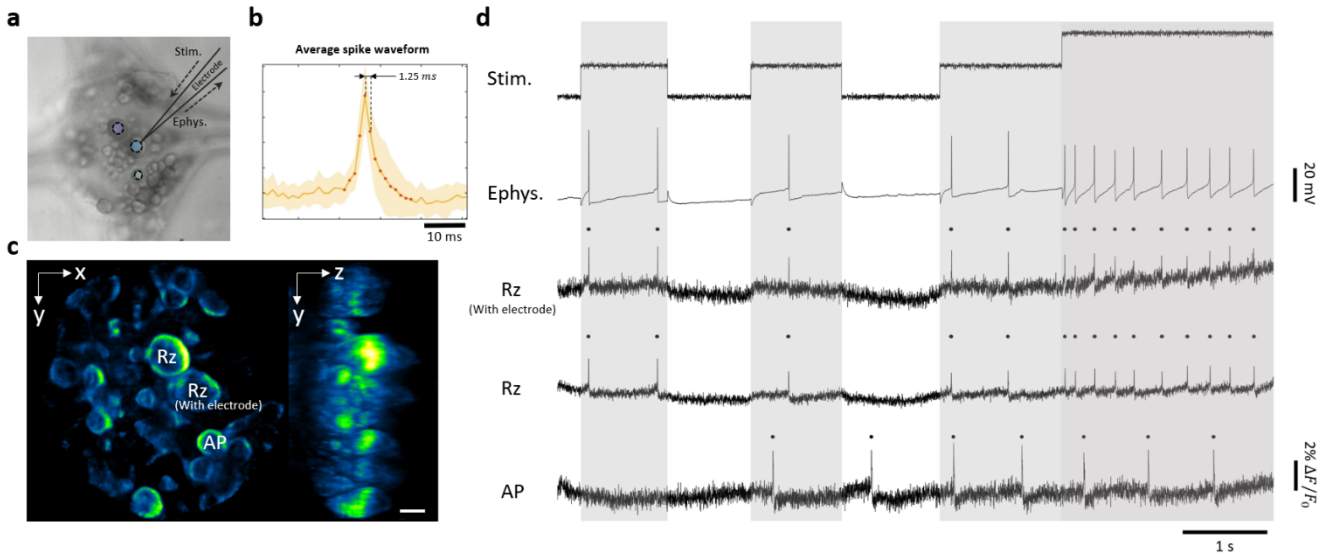

Fig. 3. 3D imaging of membrane action potentials in medicinal leech ganglions at 800 vps. a. Brightfield snapshot of leech ganglions. Microelectrode is denoted by a dotted line, which allows for simultaneous stimulation and electrophysiological recording. **b**. Average spike waveform. The yellow area marks the standard deviation of signals. Orange dots represent temporally sampling points, with an interval of $1.25\ ms$. **c**. MIP of SLIM reconstruction for voltage dye fluorescent signals. Scale bar, $50\ \mu m$. **d**. Recording of stimulation current, electrophysiological readout, and optical measurements of ganglion cells: the impaled cell (top), its contralateral partner that is electrically coupled to it (middle), and an unconnected cell (bottom). Grey boxes represent the time window when stimulation is injected. Deeper color stands for larger stimulation. Spikes are detected and marked as black dots above the traces.

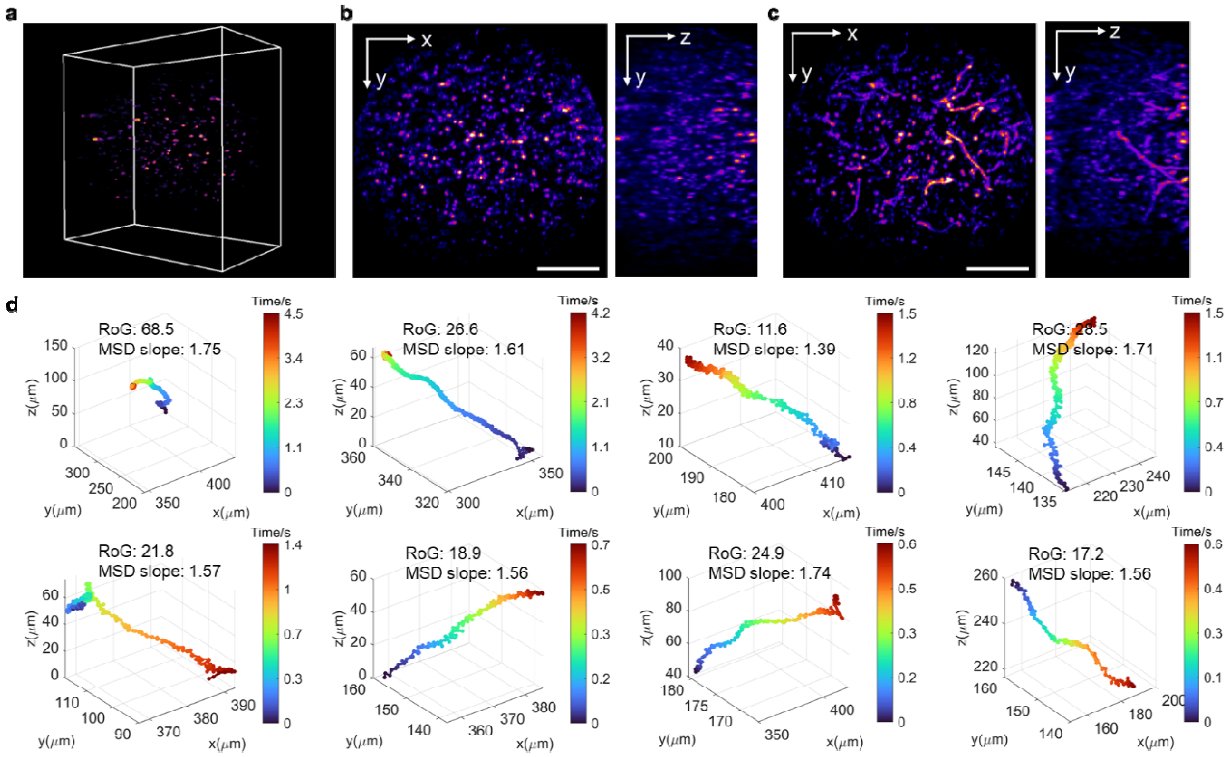

Fig. 4. 3D imaging of free-swimming *Vibrio cholerae* bacteria at 200 vps. a. 3D rendering volume of *Vibrio cholerae* bacteria. **b.** MIP from x-y and y-z slices of *Vibrio cholerae* bacteria. *Vibrio cholerae* are stained with an external membrane stain. The total recording time was 5s. **c.** MIPs of the swimming bacteria trajectory obtained by combining frames over time. **d.** Representative trajectories of swimming bacteria with their respective Radius of gyration (RoG) and Mean Squared Displacement (MSD) slopes labeled. Scale bar 50 µm.

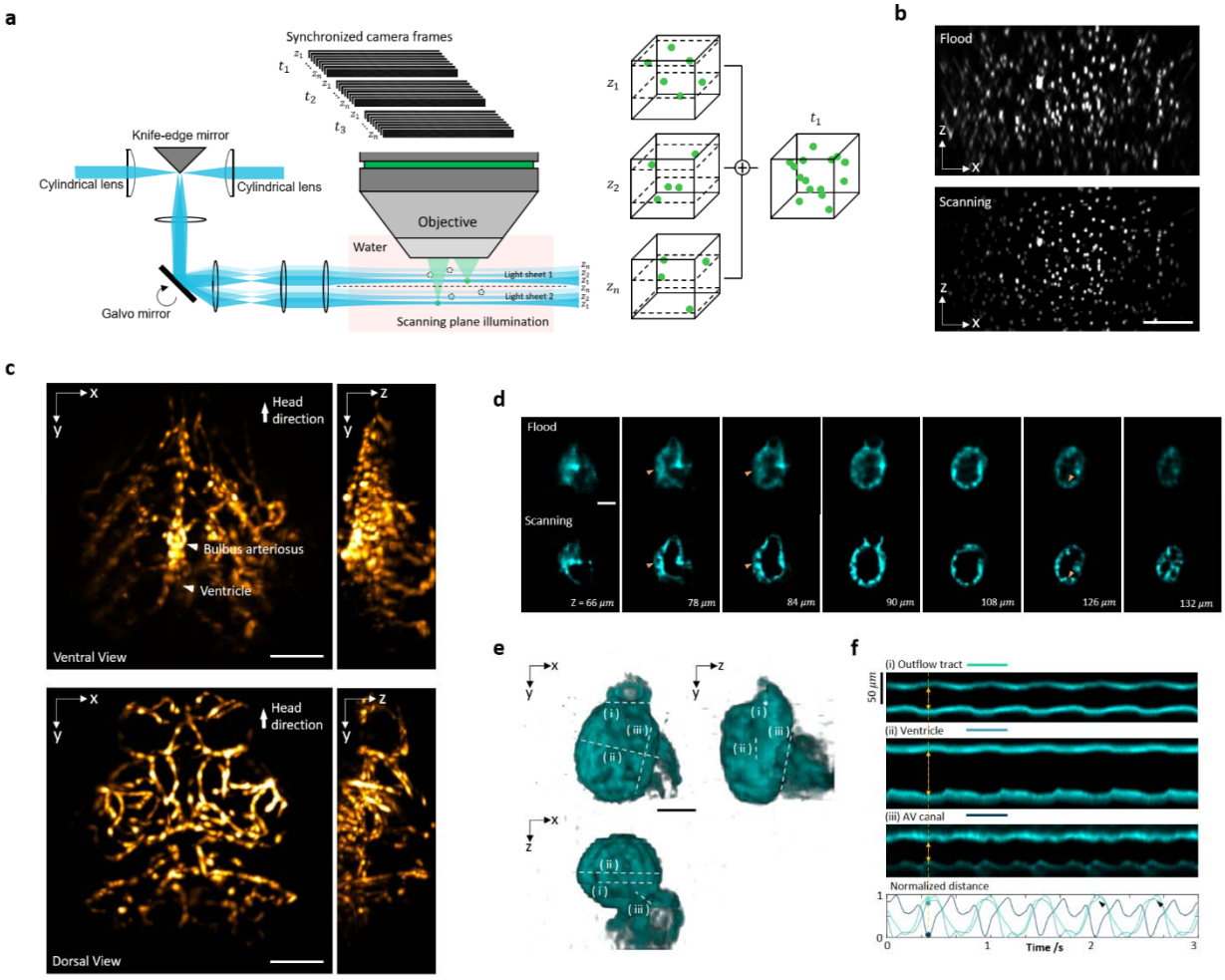

Fig. 5. 3D imaging of a beating zebrafish heart with multi-plane scanning light sheet illumination at 300 vps. a. Dual scanning light sheet replaces the flood illumination (*i.e.,* illuminating entire sample volume). In synchrony with the light sheet, the camera captures multiple frames at different scanning positions, each reconstructing two layers of the entire volume. By combining all measurements in one scan cycle, a 3D volume is synthesized for that time point. **b.** The x-z MIPs of fluorescent beads show the enhancement of image contrast and axial resolution. Scale bar, 100 μm. **c.** The structural images of the vasculature network in an embryonic zebrafish. Scale bar, 100 μm. **d**. Comparison of x-y cross-section images between scanning light sheet illumination and flood illumination on cardiomyocytes in the zebrafish heart. The orange arrows mark the muscle structures that are clearly resolved in scanning mode but challenging to flood illumination. Scale bar, $50\ \mu m$. **e.** The 3D rendering of myocardium at a representative time point. Scale bar, $50\ \mu m$. **f.** Kymographs calculated by sampling the time-dependent distance of the cavity along the white dotted line in **e**. The black arrows indicate the beat-to-beat variance of cardiac contraction. Scale bar, $50\ \mu m$.